Monthly Notices
of the
ROYAL ASTRONOMICAL SOCIETY

MNRAS **486,** 3927–3941 (2019)
Advance Access publication 2019 April 13

doi:10.1093/mnras/stz1051

Joint halo-mass function for modified gravity and massive neutrinos – I. Simulations and cosmological forecasts

Steffen Hagstotz,[1,2]★ Matteo Costanzi,[1,2] Marco Baldi[3,4,5] and Jochen Weller[1,2]

[1]*Universitäts-Sternwarte, Fakultät für Physik, Ludwig-Maximilians Universität München, Scheinerstr. 1, D-81679 München, Germany*
[2]*Excellence Cluster Universe, Boltzmannstr. 2, D-85748 Garching, Germany*
[3]*Dipartimento di Fisica e Astronomia, Alma Mater Studiorum Università di Bologna, via Gobetti 93/1, I-40129 Bologna, Italy*
[4]*Astrophysics and Space Science Observatory Bologna, via Gobetti 93/2, I-40129, Bologna, Italy*
[5]*INFN – Sezione di Bologna, viale Berti Pichat 6/2, I-40127, Bologna, Italy*

Accepted 2019 April 2. Received 2019 March 22; in original form 2018 June 19

ABSTRACT

We present a halo-mass function accurate over the full relevant Hu–Sawicki $f(R)$ parameter space based on spherical collapse calculations and calibrated to a suite of modified gravity N-body simulations that include massive neutrinos. We investigate the ability of current and forthcoming galaxy cluster observations to detect deviations from general relativity while constraining the total neutrino mass and including systematic uncertainties. Our results indicate that the degeneracy between massive neutrino and modify gravity effects is a limiting factor for the current searches for new gravitational physics with clusters of galaxies, but future surveys will be able to break the degeneracy.

Key words: galaxies: clusters – large-scale structure of Universe – neutrinos.

1 INTRODUCTION

One of the goals in modern cosmology is to understand the underlying dynamics and statistics of the cosmic density field. Clusters of galaxies trace the highest of its peaks, and theory predicts their abundance to depend exponentially on the amplitude of the matter power spectrum (Press & Schechter 1974; Bond et al. 1991; Sheth & Tormen 2002) that turns them into a formidable probe of cosmological parameters (Allen, Evrard & Mantz 2011; Kravtsov & Borgani 2012).

Studying the cosmic density field is especially of interest because it might reveal the mechanism for the observed accelerated expansion of the Universe. It can either be explained by introducing a smooth dark energy component to the Universe's energy budget, or by modifying gravity itself. Both scenarios can potentially be tested via their imprint on the abundance of clusters (Battye & Weller 2003; Mohr et al. 2003), but in this paper, we will focus on the latter.

Because general relativity (GR) is the unique theory of gravity in $1 + 3$ dimensions under very general assumptions (Lovelock 1972), any modifications introduce new physical degrees of freedom. While these can give rise to accelerated expansion, they also tend to enhance gravity at the perturbative level. One example discussed in this paper are the $f(R)$ scalar–tensor theories, which generalize the Einstein–Hilbert action by adding a non-linear function of the Ricci scalar R.

The enhancement of gravity tends to result in an increased abundance of clusters, and several approaches to model the halo-mass function in modified gravity exist (Kopp et al. 2013; Lombriser et al. 2013; Lombriser, Koyama & Li 2014; Cataneo et al. 2016; von Braun-Bates et al. 2017). But all of these studies were performed within a one-parameter extension of the minimal ΛCDM standard model, and a natural extension is the inclusion of massive neutrinos which form a small, but unknown fraction of cosmological dark matter. The detection of a non-zero neutrino mass is firmly established by particle physics as a consequence of neutrino flavour oscillations (Araki et al. 2005) and in cosmology the neutrino background can be measured in both the cosmic microwave background (CMB; Sellentin & Durrer 2015) and the large-scale structure (Baumann et al. 2018). Even though the mass scale is still uncertain, neutrinos lead to a suppression of structure growth below their free-streaming scale (Lesgourgues & Pastor 2006). This then leads to the question: Can neutrinos mask modified gravity effects in the large-scale structure? Are constraints obtained on $f(R)$ theories from cluster number counts (Schmidt, Vikhlinin & Hu 2009; Lombriser et al. 2012a; Cataneo et al. 2015) then still valid when including massive neutrinos into the analysis? And on a more fundamental level, how can the joint effects of neutrinos and modified gravity be included in the theoretical prediction of cluster abundance?

Early investigations of these issues have been presented by Baldi et al. (2014), who performed the first N-body simulations of $f(R)$ gravity in the presence of massive neutrinos, clearly demonstrating a strong degeneracy between their effects on the abundance of gravitationally bound systems. More recently, Roncarelli, Villaescusa-Navarro & Baldi (2017) and Roncarelli, Baldi & Villaescusa-

★ E-mail: steffen.hagstotz@fysik.su.se

Navarro (2018) investigated the individual impact of massive neutrinos and $f(R)$ gravity on the kinetic Sunyaev–Zeldovich signal of massive clusters, showing an opposite trend for the two models with respect to ΛCDM and thereby confirming the existence of the degeneracy. Then, Giocoli, Baldi & Moscardini (2018) and Peel et al. (2018a) explored the same degeneracies based on a combination of cluster counts and weak lensing statistics along the past light cone, while Peel et al. (2018b) and Merten et al. (2018) investigated possible methods to break these degeneracies with *machine learning* techniques. In this work, we continue investigating the combined effects of $f(R)$ and massive neutrinos by developing a theoretical model of the joint halo-mass function, calibrated to a suite of specifically designed N-body simulations.

We start with a brief summary of $f(R)$ gravity in Section 2 and present the simulation suite used to explore joint effects of modified gravity and neutrinos in Section 3. In Section 4, we introduce the joint mass function and apply our framework to forecast the ability of current and future surveys to constrain $f(R)$ theories in Section 5. We summarize our results in Section 6.

2 REVIEW OF $f(R)$ GRAVITY

We start from the modified Einstein–Hilbert action[1]

$$S = \int \mathrm{d}x^4\sqrt{-g}\left(\frac{R + f(R)}{16\pi G} + \mathcal{L}_\mathrm{m}\right), \tag{1}$$

with the Lagrangian of the matter fields $\mathcal{L}_\mathrm{m}$. We adopt the functional form proposed by Hu & Sawicki (2007)

$$f(R) = -2\Lambda\frac{R}{R + m^2}, \tag{2}$$

with a constant Λ and the curvature scale m^2. Note that $f(R) \to 0$ for $R \to 0$, in that sense the model does not contain a cosmological constant. For $m^2 \ll R$, the function can be expanded to get

$$f(R) \approx -2\Lambda - f_{R0}\frac{\bar{R}_0^2}{R}, \tag{3}$$

where $\bar{R}_0$ is the Ricci scalar today, overbars denote background quantities, and we introduced the dimensionless parameter $f_{R0} \equiv -2\Lambda m^2/\bar{R}_0^2$. To recover the well-measured ΛCDM expansion history, we fix the first term to the cosmological constant in GR $\Lambda = \Lambda_\mathrm{GR}$ and $|f_{R0}|$ is the only remaining free parameter of the model. Reproducing the standard background evolution also implies $|f_{R0}| \ll 1$, and consequently geometrical quantities are indistinguishable from ΛCDM.

The modified Einstein equations are obtained by variation of equation (1) with respect to the metric $g_{\mu\nu}$

$$G_{\mu\nu} - f_R R_{\mu\nu} - \left(\frac{f}{2} - \Box f_R\right) g_{\mu\nu} - \nabla_\mu\nabla_\nu f_R = 8\pi G T_{\mu\nu}, \tag{4}$$

with the new scalar degree of freedom $f_R \equiv \mathrm{d}f/\mathrm{d}R$. The trace of equation (4) leads to an equation of motion for the scalar field f_R

$$\nabla^2\delta f_R = \frac{a^2}{3}\left(\delta R(f_R) - 8\pi G\delta\rho_m\right), \tag{5}$$

where we adopted the quasi-static approximation and consider small perturbations on a smooth background, i.e. the quantities $\delta x \equiv x - \bar{x}$. The time–time component of the modified Einstein equations gives a Poisson-like equation for the scalar metric perturbation $2\psi = \delta g_{00}/g_{00}$

$$\nabla^2\psi = \frac{16\pi G}{3}a^2\rho_\mathrm{m} - \frac{a^2}{6}\delta R(f_R), \tag{6}$$

which can still be identified with the Newtonian potential but has contributions from both the matter density ρ_m and the scalar field via $\delta R(f_R)$. Equations (5) and (6) are non-linear and thus we will later resort to N-body simulations to solve them in general, but two limiting cases are insightful:

For large field values $|f_{R0}| \gg |\psi|$, we can linearize

$$\delta R \simeq \left.\frac{\mathrm{d}R}{\mathrm{d}f_R}\right|_{R=\bar{R}}\delta f_R, \tag{7}$$

and the Fourier-space solution of equations (5) and (6) becomes

$$k^2\psi(k) = -4\pi G\left(\frac{4}{3} - \frac{1}{3}\frac{\mu^2a^2}{k^2 + \mu^2a^2}\right)a^2\delta\rho_\mathrm{m}(k), \tag{8}$$

where we introduced the Compton wavelength of the scalar field $\mu^{-1} = (3\mathrm{d}f_R/\mathrm{d}R)^{1/2}$. On small scales $k > \mu$, this leads to a Poisson equation with an additional factor of 4/3. For scales larger than the Compton wavelength, the additional contribution vanishes and we recover behaviour as in GR.

In the opposite limit of small field values $|f_{R0}| \ll |\psi|$, the two contributions in equation (5) approximately cancel; therefore,

$$\delta R \approx 8\pi G\delta\rho_\mathrm{m} \tag{9}$$

and equation (6) turns into the usual Poisson equation. This is the *screened regime*.

To estimate where the transition occurs, we can formally solve equation (5) using the Greens's function of the Laplacian

$$\delta f_R(r) = \frac{1}{4\pi r}\frac{1}{3}\int_0^r \mathrm{d}^3\boldsymbol{r}'8\pi G\left(\delta\rho - \frac{\delta R}{8\pi G}\right) \tag{10}$$

$$= \frac{2}{3}\frac{GM_\mathrm{eff}(r)}{r} \tag{11}$$

with an effective mass M_eff as the source for field fluctuations δf_R (Schmidt 2010). Note that $M_\mathrm{eff}(r) \leq M(r)$ and equality holds in the unscreened regime where we get $\delta f_R = \frac{2}{3}\psi_\mathrm{N}$ with the Newtonial potential of a spherical overdensity $\psi_\mathrm{N} = GM/r$. Because the fluctuation in f_R is by definition smaller than its background value $\delta f_R \leq \bar{f}_R$, this translates to

$$|f_R| \leq \frac{2}{3}\psi_\mathrm{N}(r); \tag{12}$$

thus, the additional force is only sourced by mass outside of the radius where this condition is met.

To summarize, the theory is identical to ΛCDM on the background level, but perturbatively yields a maximum enhancement of gravity by one-third on scales smaller than the Compton wavelength μ^{-1}. It also includes a screening mechanism that restores GR in regions of high density and its onset is given by the typical depth of cosmological potential wells $\psi \sim 10^{-5}\ldots10^{-6}$, so that $|f_{R0}| \sim 10^{-5}\ldots10^{-6}$ is the relevant parameter space where this mechanism can function. Values of $|f_{R0}|$ below this threshold are always screened, and therefore, phenomenologically uninteresting.

3 THE DUSTGRAIN-*PATHFINDER* SIMULATIONS

For our analysis, we make use of the halo catalogues extracted from the DUSTGRAIN-*pathfinder* simulations (see Giocoli et al.

[1]We use natural units $c = \hbar = 1$.

2018, for a detailed description), a suite of cosmological *N*-body simulations designed to investigate the possible observational degeneracies between $f(R)$ gravity and massive neutrinos by sampling their joint parameter space. The simulations have a periodic box size of 750 Mpc h^{-1} per side filled with 768^3 dark matter particles of mass $m^p_{\rm cdm} = 8.1 \times 10^{10}\ {\rm M}_\odot\ h^{-1}$ (for the case of $m_\nu = 0$) and with as many neutrino particles (for the case of $m_\nu > 0$). The particles are moving under the effect of an $f(R)$ gravitational interaction mediated by the scalar potential ψ satisfying equation (6).

The DUSTGRAIN-*pathfinder* runs have been performed with the `mg-gadget` code (Puchwein, Baldi & Springel 2013) – a modified version of the GADGET code (Springel 2005) for $f(R)$ gravity theories – combined with the particle-based implementation of massive neutrinos developed by Viel, Haehnelt & Springel (2010), and already employed in Baldi et al. (2014). The `mg-gadget` $f(R)$ solver has been thoroughly tested (see e.g. Winther et al. 2015) and already used for several applications in cosmology ranging from pure collisionless simulations (Baldi & Villaescusa-Navarro 2018; Arnold et al. 2019) to hydrodynamical simulations (Arnold, Puchwein & Springel 2015; Roncarelli et al. 2018), to zoomed simulations of Milky Way-sized objects (Arnold, Springel & Puchwein 2016; Naik et al. 2018).

Initial conditions have been produced by generating two separate but fully correlated random realizations of the linear density power spectrum for CDM and massive neutrino particles as computed by the Einstein–Boltzmann code CAMB (Lewis, Challinor & Lasenby 2000) at the starting redshift of the simulation $z_{\rm i} = 99$. Following the approach of e.g. Zennaro et al. (2017) and Villaescusa-Navarro et al. (2018), neutrino gravitational velocities are calculated based on the scale-dependent growth rate $D(z_i, k)$ for the neutrino component. On top of these, neutrino particles also receive an additional thermal velocity extracted from the neutrino momentum distribution for each value of neutrino mass under consideration.

In this work – which is the third in a series of papers making use of the DUSTGRAIN-*pathfinder* simulations after Giocoli et al. (2018) and Peel et al. (2018a) – we restrict our focus on a subset of the full simulations suite consisting of nine runs whose parameters are summarized in Table 1. All simulations share the same standard cosmological parameters that are set in accordance with the Planck 2015 constraints (Planck Collaboration XIII 2016a), namely $\Omega_{\rm m} = \Omega_{\rm cdm} + \Omega_{\rm b} + \Omega_\nu = 0.31345$, $\Omega_{\rm b} = 0.0481$, $\Omega_\Lambda = 0.68655$, $H_0 = 67.31\ {\rm km\ s^{-1}\ Mpc^{-1}}$, $\mathcal{A}_{\rm s} = 2.199 \times 10^{-9}$, $n_{\rm s} = 0.9658$.

For all simulations, we have identified collapsed CDM structures in each comoving snapshot by means of a friends-of-friends (FoF) algorithm (see Davis et al. 1985) on the CDM particles with linking length $\lambda = 0.16 \times d$, where d is the mean interparticle separation, retaining only structures with more than 32 particles. On top of such FoF catalogue, we have run the SUBFIND algorithm (Springel et al. 2001) to identify gravitationally bound structures and to associate standard quantities such as the mass and the radius to the main substructure of each FoF group. The latter quantities are computed in the usual way by growing spheres of radius R around the most-bound particle of each main substructure enclosing a total mass M until the condition

$$\frac{4}{3}\pi R^3_{200m} \times 200 \times \Omega_{\rm m}\rho_{\rm crit} = M_{200m} \tag{13}$$

is fulfilled for $R = R_{200m}$ and $M = M_{200m}$, where $\rho_{\rm crit} \equiv 3H^2/8\pi G$ is the critical density of the universe.

4 JOINT MASS FUNCTION

Dark matter haloes form from collapsing regions that decouple from the background expansion. Their abundance can be related to the volume fraction of the initially Gaussian density field δ_R smoothed on a radius R above a critical collapse threshold $\delta_{\rm c}$ (Press & Schechter 1974). This yields the number density of haloes within a mass interval $[M, M + {\rm d}M]$, the halo-mass function:

$$\frac{{\rm d}n}{{\rm d}M} = f(\sigma)\frac{\rho_{\rm m}}{M^2}\frac{{\rm d}\ln\sigma^{-1}}{{\rm d}\ln M}, \tag{14}$$

where $\rho_{\rm m} = \Omega_{\rm m}\rho_{\rm crit}$ is the mean density of the Universe and $f(\sigma)$ is the multiplicity function related to the collapsed volume fraction $F(M)$ occupied by haloes over mass M by

$$f(\sigma) = 2\sigma^2\partial F/\partial\sigma^2\,. \tag{15}$$

It depends on the variance of the linear density field

$$S \equiv \sigma^2\big(R(M), z\big) = \int \frac{{\rm d}k}{k}\frac{k^3P(k,z)}{2\pi^2}W^2\big(kR(M)\big) \tag{16}$$

within a filter W containing the mass $M = 4/3\pi R^3\rho_{\rm m}$. The variables M, R, and σ^2 are monotonous functions of each other and can therefore be used interchangeably.

Note that even though σ is often thought of as growing with cosmic time $\sigma(z) = D(z)\sigma_0$, in the framework of spherical collapse it is instructive to consider the threshold $\delta_{\rm c}(z) = \delta_{\rm c}/D(z)$ as the dynamical quantity. At early times, the density field is Gaussian and completely characterized by its variance alone. The collapse criterion is then really a criterion imposed on the *initial conditions*.

If we assume a top-hat filter in Fourier space $W = \theta(k - 1/R)$, each new mode of the density field entering the filter is independent and the smoothed field performs a random walk with R (or equivalently S) as a time variable. The problem can then be rephrased: when does a trajectory $\delta(S)$ first cross the threshold $\delta_{\rm c}$ (Bardeen et al. 1986; Bond et al. 1991)?

Under these assumptions individual trajectories follow a Langevin equation

$$\frac{\partial\delta}{\partial S} = \eta(S)\,, \tag{17}$$

with a stochastic driving term η defined by its mean $\langle\eta\rangle = 0$ and variance $\langle\eta(S)\eta(S')\rangle = \delta_D(S - S')$. The probability distribution Π of trajectories then evolves according to the corresponding Fokker–Planck equation

$$\frac{\partial\Pi}{\partial S} = \frac{1}{2}\frac{\partial^2\Pi}{\partial\delta^2}\,, \tag{18}$$

with the boundary condition $\Pi(\delta,\ S = 0) = \delta_D(\delta)$ because the Universe is homogeneous on large scales. However, trajectories can cross the barrier more than once leading to double-counting of haloes. To solve this, one demands the additional boundary condition (an absorbing barrier) $\Pi(\delta = \delta_{\rm c}, S) = 0$.

The solution to equation (18) is then given by (Bond et al. 1991)

$$\Pi(\delta, \sigma^2) = \frac{1}{2\pi\sigma^2}\left({\rm e}^{-\delta^2/2\sigma^2} - {\rm e}^{-(2\delta_{\rm c}-\delta)^2/2\sigma^2}\right)\,, \tag{19}$$

where the second Gaussian term reflects the fact that trajectories end at the barrier. Omitting it lead to the missing normalization factor of 2 of the Press & Schechter (1974) prediction.

With the boundary condition, the distribution function vanishes for $\delta > \delta_{\rm c}$, so we express $F(S)$ by subtracting the fraction of

Table 1. The subset of the DUSTGRAIN-*pathfinder* simulations considered in this work with their specific parameters.

Simulation name	Gravity type	$\lvert f_{R0}\rvert$	$\sum m_\nu$ (eV)	$\Omega_{\rm cdm}$	Ω_ν	$m^p_{\rm cdm}$ ($\mathrm{M}_\odot\, h^{-1}$)	m^p_ν ($\mathrm{M}_\odot\, h^{-1}$)
ΛCDM	GR	–	–	0.31345	–	8.1×10^{10}	–
fR4	$f(R)$	10^{-4}	–	0.31345	–	8.1×10^{10}	–
fR5	$f(R)$	10^{-5}	–	0.31345	–	8.1×10^{10}	–
fR6	$f(R)$	10^{-6}	–	0.31345	–	8.1×10^{10}	–
fR4-0.3eV	$f(R)$	10^{-4}	0.3	0.30630	0.00715	7.92×10^{10}	1.85×10^{9}
fR5-0.15eV	$f(R)$	10^{-5}	0.15	0.30987	0.00358	8.01×10^{10}	9.25×10^{8}
fR5-0.1eV	$f(R)$	10^{-5}	0.1	0.31107	0.00238	8.04×10^{10}	6.16×10^{8}
fR6-0.1eV	$f(R)$	10^{-6}	0.1	0.31107	0.00238	8.04×10^{10}	6.16×10^{8}
fR6-0.06eV	$f(R)$	10^{-6}	0.06	0.31202	0.00143	8.07×10^{10}	3.7×10^{8}

trajectories that did not yet cross the threshold

$$F(\sigma^2) = 1 - \int_{-\infty}^{\delta_c} \Pi(\delta, \sigma^2)\mathrm{d}\delta\,, \tag{20}$$

from which we can derive the multiplicity function $f(\sigma)$ by using equation (15) to get the mass function by Press & Schechter (1974)

$$f_k(\sigma) = \sqrt{\frac{2}{\pi}}\frac{\delta_c}{\sigma}\mathrm{e}^{-\delta_c^2/(2\sigma^2)}, \tag{21}$$

with the correct normalization. Note that we indicate solutions from non-correlated random walks (using a k-space top-hat) with subscript k.

This approach works reasonably well, but has several shortcomings:

(i) Collapse in a Gaussian random field does not occur spherically. In the Zel'dovich approximation, the eigenvalues λ_i of the deformation tensor follow the joint probability distribution (Doroshkevich 1970)

$$p(\lambda_1, \lambda_2, \lambda_3) = \frac{15^3}{8\pi\sqrt{5}\sigma^6}\exp\left(-\frac{3I_1^2}{\sigma^2} + \frac{15I_2}{2\sigma^2}\right) \tag{22}$$

$$\times\ |(\lambda_3 - \lambda_2)(\lambda_3 - \lambda_1)(\lambda_2 - \lambda_1)|\,, \tag{23}$$

with $I_1 = \lambda_1 + \lambda_2 + \lambda_3$ and $I_2 = (\lambda_1\lambda_2 + \lambda_1\lambda_3 + \lambda_2\lambda_3)$. Isotropic collapse with $\lambda_1 = \lambda_2 = \lambda_3$ therefore does not occur. Instead, the Zel'dovich picture suggests a collapse into subsequently walls, sheets, filaments, and haloes, where the last step occurs typically along a filament in an ellipsoidal fashion. This is fully consistent with structure formation observed in N-body simulations.

(ii) Real haloes do not form out of sharp k-space top-hats. Usually, one assumes rather a real-space top-hat as initial condition for the spherical collapse. This leads to coupling of Fourier modes and introduces correlations between steps of the random walk.

4.1 Diffusing, drifting barrier

The non-spherical collapse dynamics can be addressed by modifying the collapse barrier. The main motivation is that low-mass (high σ) haloes are more ellipsoidal, while the largest objects are approximately spherical. Ellipsoidal patches collapse later because they have to get rid of angular momentum, which leads to an effective higher threshold. There are various ways to extend the excursion set formalism to account for this, and here we follow Kopp et al. (2013) and introduce a scale-dependent barrier of the form

$$B = \delta_c + \beta S\,, \tag{24}$$

which tends to the spherical collapse threshold δ_c for high-mass haloes $\sigma \ll 1$. Even though more general forms for the ellipsoidal collapse barrier B can be found in the literature (e.g. $B = \delta_c + \beta S^\gamma$; see Sheth & Tormen 2002), the linear approximation adopted in this work is sufficient for typical cluster abundance studies using clusters of mass $M \gtrsim 10^{13.5}\,\mathrm{M}_\odot\, h^{-1}$.

In addition to the barrier drift, the collapse dynamics themselves are complicated by environmental effects and fuzzy halo definitions. In Maggiore & Riotto (2010b), this was taken into account by turning the barrier itself into a Gaussian stochastic variable with a mean $\bar{B} = \delta_c + \beta S$ and width D_B. Both the trajectories and the barrier itself perform a random walk, and the joint probability distribution is obtained from a 2D Fokker–Planck equation (Maggiore & Riotto 2010b; Corasaniti & Achitouv 2011)

$$\frac{\partial\Pi}{\partial S} = \frac{1}{2}\frac{\partial^2\Pi}{\partial\delta^2} + \frac{D_B}{2}\frac{\partial^2\Pi}{\partial B^2}\,, \tag{25}$$

which leads to the multiplicity

$$f_k(\sigma) = \sqrt{\frac{2a}{\pi}}\frac{1}{\sigma}\mathrm{e}^{-a\bar{B}^2/(2\sigma^2)}\left(\bar{B} - \sigma^2\frac{\mathrm{d}\bar{B}}{\mathrm{d}\sigma^2}\right), \tag{26}$$

with $a \equiv 1/(1 + D_B)$. Using equation (24), this reduces to a Press–Schechter like solution with the constant threshold δ_c replaced by the full barrier:

$$f_k(\sigma) = \sqrt{\frac{2a}{\pi}}\frac{\delta_c}{\sigma}\mathrm{e}^{-a(\delta_c+\beta\sigma^2)^2/2\sigma^2}. \tag{27}$$

A broader barrier D_B then leads to a smaller factor a in the exponential, boosting the abundance of high-mass clusters because those rare trajectories can cross the threshold more easily.

4.2 Non-Markovian corrections

Accounting for realistic filter functions makes it necessary to consider the deviations from an uncorrelated random walk. Haloes form from regions that resemble spherical patches in the initial conditions and several possible window functions to capture the correct form of these proto-haloes exist (Bond et al. 1991). Here, we assume a real space top-hat, which in Fourier space turns into

$$W(x) = \frac{3j_1(x)}{x}\,, \tag{28}$$

with the spherical Bessel function j_1, which we use from here on to calculate the variance of the density field S in equation (16). In Maggiore & Riotto (2010a), the authors calculated the corrections induced by correlations between the variance S smoothed at different radii R for this choice of smoothing filter. The general two-point correlation function can be written as

$$\langle\delta_1\delta_2\rangle = \min(S_1, S_2) + \Delta(S_1, S_2)\,, \tag{29}$$

where we introduced the shorthand $\delta_1 = \delta(R_1)$, and the first term expresses the Markov dynamics leading to the Press–Schechter result with a general barrier in equation (27). The correction is of the form

$$\Delta(S_1, S_2) = \kappa \frac{S_1(S_2 - S_1)}{S_2} \tag{30}$$

with the correlation coefficient fitted to numerical ΛCDM results (Maggiore & Riotto 2010a)

$$\kappa(R) \simeq 0.459 - 0.003R\,, \tag{31}$$

and has a weak dependence on cosmology via the power spectrum. As pointed out above, we deal with a purely Gaussian field in the initial conditions here, and all correlations are introduced by the filter and not by later non-linear mode coupling. This also means that κ should be calculated from the ΛCDM relation in equation (31) even within a modified gravity model. We will return to this point when discussing the modified gravity mass function.

This leads to the real-space top-hat multiplicity function f_x to the first order in the correlation coefficient κ (Maggiore & Riotto 2010a; Kopp et al. 2013),

$$f_x(\sigma) \approx f_k(\sigma) + \kappa \left(f^{m-m}_{\beta^{(0)}}(\sigma) + f^{m-m}_{\beta^{(1)}}(\sigma) + f^{m-m}_{\beta^{(2)}}(\sigma) \right) \tag{32}$$

with the Markovian (i.e. $\kappa = 0$) term f_k for a diffusive, drifting barrier given by equation (27) and the memory-of-memory corrections (Corasaniti & Achitouv 2011) themselves are expanded up to the second order in the drift parameter β to get

$$f^{m-m}_{\beta^{(0)}}(\sigma) = a\frac{\delta_c}{\sigma}\left(e^{a\delta_c^2/2\sigma^2} - \frac{1}{2}\Gamma\left(0, \frac{a\delta_c^2}{2\sigma^2}\right)\right), \tag{33}$$

$$f^{m-m}_{\beta^{(1)}}(\sigma) = -a\delta_c\beta\left(a\,\mathrm{erfc}\left(\delta_c\sqrt{\frac{a}{2\sigma^2}}\right) + f^{m-m}_{\beta^{(0)}}(\sigma)\right), \tag{34}$$

$$f^{m-m}_{\beta^{(2)}}(\sigma) = -a\beta\left(\frac{\beta}{2}\sigma^2 f^{m-m}_{\beta^{(0)}}(\sigma) + \delta_c f^{m-m}_{\beta^{(1)}}(\sigma)\right), \tag{35}$$

where $\mathrm{erfc}(x)$ is the complementary error function and $\Gamma(0, x)$ denotes the incomplete Gamma function.

4.3 Spherical collapse in modified gravity

As for the ΛCDM case, the starting point of our analysis is spherical collapse. Kopp et al. (2013) numerically solved the full modified Einstein, scalar field, and non-linear fluid equations to obtain δ_c in $f(R)$ gravity, and they parametrized their solution for the threshold by

$$\delta_c^{f(R)}(f_{R0}, M, z) = \delta_c^{\mathrm{GR}}(z) \times \Delta(f_{R0}, M, z)\,, \tag{36}$$

where the deviation from GR is captured by the correction factor

$$\Delta(f_{R0}, M, z) = 1 + b_2(1+z)^{-a_3}\left(m_b - \sqrt{m_b^2 + 1}\right) + b_3(\tanh(m_b) - 1), \tag{37}$$

Table 2. Fiducial values for the GR mass function barrier shape and the virial $f(R)$ collapse threshold equation (36).

GR	$f(R)$				
D_B	β	α_4	β_3	μ_1	μ_2
0.4	0.12	0.11	2.7×10^{-3}	1.99	26.21

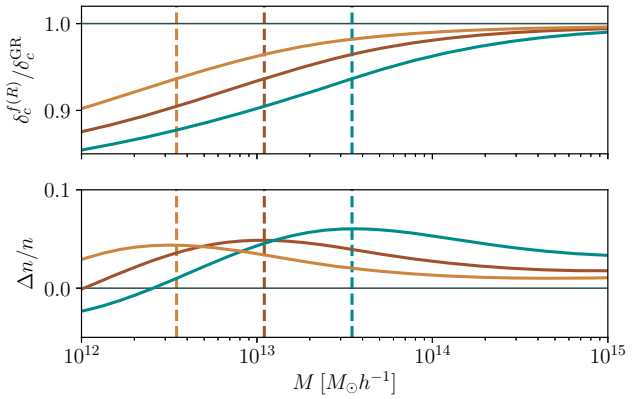

Figure 1. Top: Relative change in the collapse threshold $\delta_c/\delta_c^{\mathrm{GR}}$ for slightly different values of the screening mass M_{screen} (dashed vertical lines) around $|f_{R0}| \simeq 10^{-6}$ at $z = 0$. This corresponds to the position of the typical bump in the relative cluster abundance compared to ΛCDM (bottom).

$$\begin{aligned} m_b(f_{R0}, M, z) &= (1+z)^{a_3}\left(\log_{10} M - m_1(1+z)^{-a_4}\right), \\ m_1(f_{R0}) &= \mu_1 \log_{10}|f_{R0}| + \mu_2, \\ b_2 &= 0.0166, \\ b_3(f_{R0}) &= \beta_3\left(2.41 - \log_{10}|f_{R0}|\right), \\ a_3(f_{R0}) &= 1 + \exp\left(-2.08\left(\log_{10}|f_{R0}| + 5.56\right)^2\right), \\ a_4(f_{R0}) &= \alpha_4(\tanh(0.69(\log_{10}|f_{R0}| + 6.65)) + 1). \end{aligned} \tag{38}$$

The parametrization converges to the GR limit δ_c^{GR} separately for high z and $|f_{R0}| \to 0$, which is well approximated by (Nakamura & Suto 1997)

$$\delta_c^{\mathrm{GR}}(z) = \frac{3(12\pi)^{2/3}}{20}\left(1 - 0.0123\log_{10}\left(1 + \frac{\Omega_m^{-1} - 1}{(1+z)^3}\right)\right). \tag{39}$$

The coefficients in equation (37) were fitted to numerical solutions of the collapse dynamics, and we will focus on $\alpha_4, \beta_3, \mu_1, \mu_2$ whose fiducial values from Kopp et al. (2013) are given in Table 2.

The crucial ingredient to calculate the $f(R)$ threshold is m_b, which sets the transition mass where screening sets in. We will express this scale as the screening mass M_{screen}, defined by $m_b(M_{\mathrm{screen}}) = 0$. In Fig. 1, we show the connection between the threshold and the cluster abundance: the threshold grows quasi-linearly with $\log M$ up to the inflexion point M_{screen}, after which δ_c asymptotically reverts to the fiducial GR value. In the mass function, this scale corresponds to a characteristic peak in the additional relative abundance. Note that the negative relative abundance for lower masses shown in the plot is physical because of mass conservation: additional high-mass objects form from low-mass haloes. Different background densities Ω_m will lead to slightly different screening behaviour, so this description should only be used in proximity to matter densities implied by the CMB.

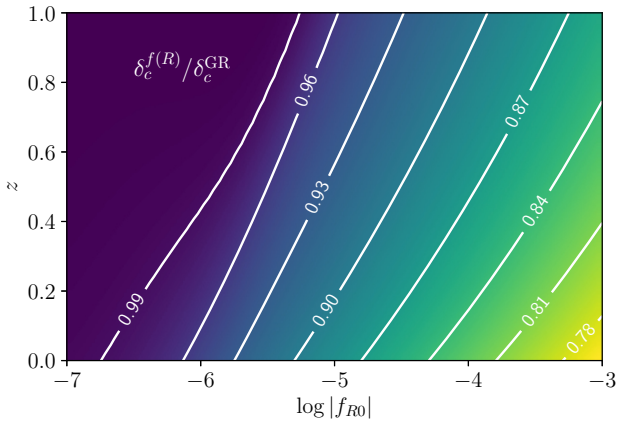

Figure 2. Change in collapse threshold $\delta_c^{f(R)}/\delta_c^{\rm GR}$ for a halo of fixed mass $M_{200} = 10^{14}\,{\rm M}_\odot\,h^{-1}$ with redshift for various values of $|f_{R0}|$. The fiducial threshold is lowered due to the fifth force for large $|f_{R0}|$. At high redshifts, $\delta_{\rm c}$ reverts to the ΛCDM value. The plot includes the corrections from Section 4.6.

For $m_b = 0$, the threshold is given by

$$\delta_{\rm c} = \delta_{\rm c}^{\rm GR}\left(1 + b_2(1+z)^{-a_3} - b_3\right), \tag{40}$$

and because a lower $\delta_{\rm c}$ leads to a higher cluster abundance, b_2 and b_3 set the height of the additional abundance peak, a_3 and a_4 control the redshift evolution of the screening mass, and μ_1, μ_2 determine how quickly the model reverts to GR when changing f_{R0}.

Fig. 2 shows the variation of the threshold as a function of redshift for various values of the $|f_{R0}|$ parameter, assuming a halo with $M_{200} = 10^{14}\,{\rm M}_\odot\,h^{-1}$. Considering this mass representative of the lightest objects entering a cosmological cluster catalogue, the leftmost line indicates the limit of cluster abundance studies to constrain the theory at a given redshift where the deviation in $\delta_{\rm c}$ is of order 1 per cent.[2]

To write the multiplicity function for $f(R)$ including non-Markovian corrections, we assume that the correlation between steps behaves similar for modified gravity and GR. This is justified because we measure the correlation in the initial conditions where the density fields in both theories are identical – all modifications to the time evolution are absorbed into the threshold $\delta_{\rm c}(f_{R0}, M, z)$. Therefore, we write (Kopp et al. 2013)

$$f_x^{f(R)}(\sigma) \simeq f_x^{\rm GR}(\sigma)\frac{f_k^{f(R)}}{f_k^{\rm GR}} \tag{41}$$

with the Markovian multiplicity function $f_k^{f(R)}$ derived from the modified gravity barrier $\bar{B} = \delta_{\rm c}(f_{R0}, M, z) + \beta\sigma^2$ given in equation (36)

$$\begin{aligned} f_k^{f(R)}(\sigma) &= \sqrt{\frac{2a}{\pi}}\frac{1}{\sigma}{\rm e}^{-a\bar{B}^2/(2\sigma^2)}\left(\bar{B} - \sigma^2\frac{{\rm d}\bar{B}}{{\rm d}\sigma^2}\right) \\ &= \sqrt{\frac{2a}{\pi}}\frac{1}{\sigma}{\rm e}^{-a\bar{B}^2/(2\sigma^2)}\left(\delta_{\rm c}^{f(R)} - \frac{3M}{2}\frac{\partial\delta_{\rm c}^{f(R)}}{\partial M}\frac{\partial\ln\sigma}{\partial\ln R}\right). \end{aligned} \tag{42}$$

Together with $f_k^{\rm GR}$ (equation 27) and $f_x^{\rm GR}$ (equation 32), this defines the full modified gravity multiplicity function (equation 41) and yields the halo-mass function via equation (14). We emphasize again that all expressions are defined for the smoothed density field $\sigma^{\rm GR}$ calculated in a *standard cosmology* – as already discussed, the threshold is imposed on the initial conditions, and all subsequent effects of modified gravity are encapsulated in the dynamics of the barrier.

[2]Even though a given uncertainty in $\delta_{\rm c}$ does not translate to the mass function linearly, our approach models correction to the threshold; therefore, once it is too close to GR, it cannot be used to constrain deviations anymore.

4.4 Neutrinos

As we have seen, the signal of modified gravity is a lower collapse threshold and a resulting higher abundance of clusters compared to ΛCDM. To set realistic limits on deviations from GR, we will now incorporate effects of massive neutrinos. As has been studied before (see e.g. Lesgourgues & Pastor 2006), they suppress structure growth below the free-streaming scale that leads to a lower abundance of galaxy clusters, counteracting possible effects of $f(R)$. Constraining the neutrino mass is an important goal for cluster cosmology in its own right, but here we will focus on degeneracy with modified gravity effects.

Ichiki & Takada (2012), Costanzi et al. (2013), and Castorina et al. (2014) showed that the effect of neutrinos on the cluster abundance can be well captured by rescaling the smoothed density field

$$\sigma^2 \to \sigma^2_{\rm cdm}(z) = \int\frac{{\rm d}k}{k}\frac{k^3 P_{\rm cdm}(k,z)}{2\pi^2}\,W^2(kR), \tag{43}$$

with the CDM power spectrum obtained by rescaling the total matter power spectrum $P_{\rm m}$ with the respective transfer functions weighted by the density of each species

$$P_{\rm cdm}(k,z) = P_{\rm m}(k,z)\left(\frac{\Omega_{\rm cdm}T_{\rm cdm}(k,z) + \Omega_{\rm b}T_{\rm b}(k,z)}{T_{\rm m}(k,z)(\Omega_{\rm cdm}+\Omega_{\rm b})}\right)^2, \tag{44}$$

thus assuming that neutrinos are distributed smoothly on cluster scales. The scale dependent growth caused by neutrinos for the other components is also accounted for by the transfer functions. Equation (43) is expressed as a time-dependent rescaling, but we can also again think of the initial density field as fixed and map the change to the collapse threshold

$$\delta_{\rm c}^{\nu} = \frac{\sigma(z)}{\sigma_{\rm cdm}(z)}\delta_{\rm c}. \tag{45}$$

In this picture, we account for the effect of neutrinos by introducing an appropriate shift in the time variable σ^2 of the random walk. This rescaling expresses the cold dark matter (CDM) approximation outlined above and it allows us to compare the effects of modified gravity and neutrinos on the threshold directly. While there is some ambiguity how to compare cosmologies with and without neutrinos, in this paper we choose to keep the total matter density $\Omega_{\rm m}$ fixed. Thus when adding neutrinos, we rescale the dark matter density by (Lesgourgues & Pastor 2006)

$$\Omega'_{\rm cdm} = \Omega_{\rm cdm} - \frac{\sum m_\nu}{93.14\ {\rm eV}}. \tag{46}$$

In Fig. 3, we show the rescaled critical density for collapse δ_c^{ν} and the resulting effect on the halo-mass function. A larger $\delta_{\rm c}$ leads to an increased exponential suppression of high-mass haloes in equation (26). Note that the scale dependent growth caused by neutrinos translates to a weak mass dependence of the barrier. To check how this suppression can mask the additional abundance caused by modified gravity, we combine the $f(R)$ threshold with the neutrino rescaling from equation (45):

$$\delta_{\rm c}^{\rm eff} = \frac{\sigma(z)}{\sigma_{\rm cdm}(z)}\delta_{\rm c}^{f(R)}. \tag{47}$$

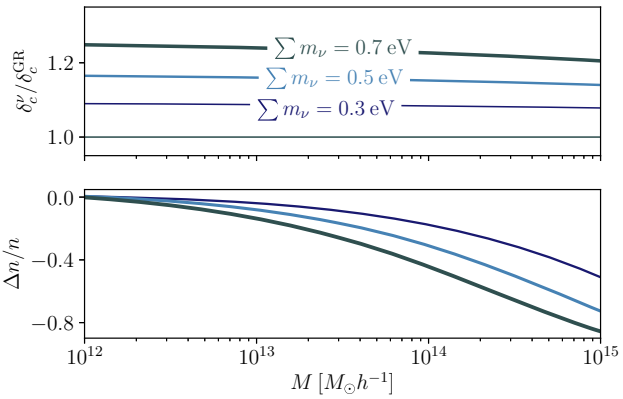

Figure 3. Top: Change in the collapse threshold δ_c^ν/δ_c for different neutrino masses. The scale-dependent growth in νCDM cosmologies translates to a slight mass dependence of δ_c. The higher threshold leads then to a stronger suppression in the exponential high-mass tail of the mass function (bottom).

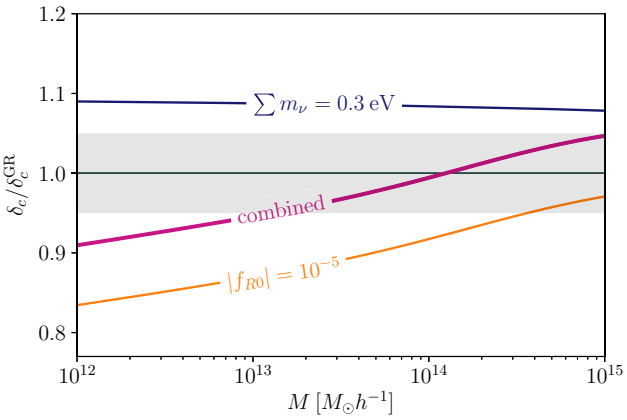

Figure 4. Change in the effective collapse threshold at $z = 0$ induced by massive neutrinos with $\sum m_\nu = 0.3$ eV (blue), for $|f_{R0}| = 10^{-5}$ (orange) and the combined effect. The grey shaded region shows a 5 per cent deviation from the fiducial value. Over the mass range $M > 10^{14}\,\mathrm{M}_\odot h^{-1}$ relevant for cluster abundance studies, the effects of neutrinos and modified gravity are approximately degenerate.

A suitable combination of neutrino masses and $|f_{R0}|$ can then lead to an effective barrier close to its ΛCDM value over the mass range $M > 10^{14}\mathrm{M}_\odot h^{-1}$ relevant for cluster surveys, as demonstrated in Fig. 4. We will return to this point and check the validity of this approach by comparing to simulations in Section 4.6.

4.5 Halo bias and cluster clustering

The mass function also allows us to derive the corresponding clustering bias. The Eulerian bias is given by the overabundance of objects in a region with an overdensity δ_0 compared to the mean abundance (Sheth & Tormen 1999)

$$b = 1 + \frac{1}{\bar{n}(M)}\frac{\mathrm{d}\bar{n}(M|\delta_0)}{\mathrm{d}\delta_0} = 1 + \frac{1}{f(\sigma)}\left.\frac{\mathrm{d}f(\sigma|\delta_0,\sigma_0)}{\mathrm{d}\delta_0}\right|_{\delta_0=0}; \quad (48)$$

therefore, the first-order bias is the linear response of the halo field to changes in the underlying density field. For a fixed barrier, the conditional mass function $f(\sigma|\delta_0)$ simply involves a shift of the barrier $\delta_c \to \delta_c$–δ_0, but for a generic barrier the situation is more complicated.

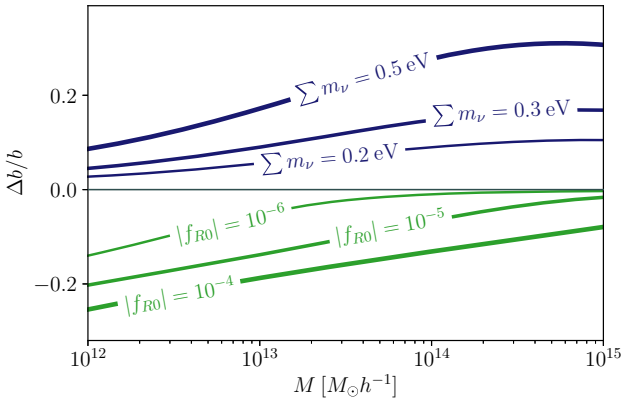

Figure 5. Deviations from the fiducial GR bias for several values of $|f_{R0}|$ and $\sum m_\nu$ at redshift $z = 0$. Clusters become more abundant with larger values of $|f_{R0}|$, so they become less biased. For neutrinos this trend is reversed, the suppression of high-mass objects increases their bias.

Achitouv et al. (2016) proposed the conditional mass function for a generic barrier

$$f(S|\delta_0, S_0) = \sqrt{\frac{2}{\pi}}\left(\bar{B} - S\frac{\mathrm{d}\bar{B}}{\mathrm{d}S} + \frac{S^2}{2}\frac{\mathrm{d}^2\bar{B}}{\mathrm{d}S^2} - \delta_0\right)\frac{S/a}{(S/a - S_0)^{3/2}} \quad (49)$$

$$\times \exp\left(-\frac{(\bar{B} - \delta_0)^2}{2(S/a - S_0)}\right), \quad (50)$$

and found good agreement with Monte Carlo random walks for various barrier shapes. This yields the linear bias

$$b(S) = 1 + \left(\frac{a\bar{B}}{S} - \frac{1}{\bar{B} - S\frac{\mathrm{d}\bar{B}}{\mathrm{d}S}}\right), \quad (51)$$

with the same barrier $\bar{B}$ used for the mass function, but the bias depends only mildly on the barrier width D_B and drift β for the mass range we focus on in this work. It is mainly sensitive to the mean threshold δ_c.

We show the changes in the bias induced by modified gravity or massive neutrinos in Fig. 5, using the $f(R)$ barrier $\bar{B}(M, z, f_{R0})$. The lower threshold means that clusters form out of smaller overdensities compared to ΛCDM, so they are less biased tracers of the density field. This tendency is only enhanced the stronger the $f(R)$ effect gets and the linear bias shrinks with larger values of $|f_{R0}|$. For neutrinos, this effect is reversed: because the high-mass tail of the mass function is suppressed, massive clusters are less abundant overall and therefore only form in very overdense regions. However, the absolute scale of the halo bias in ΛCDM is still uncertain (Baxter et al. 2016; Paech et al. 2017), making it very difficult to use this behaviour for constraints – both neutrinos and modified gravity lead to a lower bias of low-mass objects compared to high-mass objects. We therefore leave a forecast analysis also including the clustering of clusters for future work.

4.6 Calibration and comparison

The excursion set framework predicts the mass function in terms of the halo mass at virialization $\mathrm{d}n/\mathrm{d}M_\mathrm{vir}$, since this is the time at which the halo stops to collapse. Moving to modified gravity, the virial overdensity is even more complicated. While constant in an

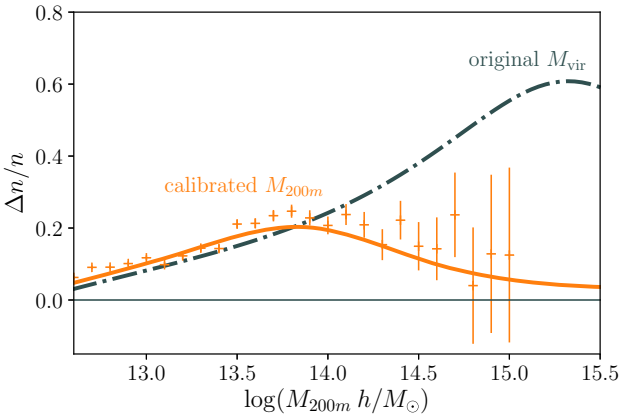

Figure 6. Relative simulated M_{200m} halo abundance for $|f_{R0}| = 10^{-5}$ at redshift $z = 0.3$ compared with the original spherical collapse prediction for virial masses (grey, dot–dashed) and our calibrated model (orange, solid). We assume Poisson errors for the simulated counts.

Einstein-de-Sitter universe, we expect $\Delta_{\rm vir}^{f(R)}$ to evolve with f_{R0}, $\Omega_{\rm m}$, and redshift.

From the observational point of view, however, the mass of a cluster is often defined as the mass inside a sphere encompassing an overdensity Δ times a reference value. In this work, we adopt $\Delta_{\rm m} = 200$ with respect to the mean matter density as given in equation (13) to define our simulated catalogues and calibrate the mass function accordingly.

A first exemplary comparison between the fiducial barrier model equation (36) and our simulation is shown in Fig. 6 for $f_{R0} = 10^{-5}$ and $z = 0.3$. The virial mass function from Kopp et al. (2013) is a bad fit to the M_{200m} catalogue for masses beyond $\sim 10^{14}\,{\rm M}_\odot\,h^{-1}$ since the screening mass is offset, leading to a wrong position and amplitude of the $f(R)$ bump. To calibrate the mass function to a new mass definition, we focus on the screening mass m_b in equation (38). We keep the functional form, but because the position and evolution of the screening mass scale is different for another mass definition, we re-fit the parameters μ_1, μ_2 to account for the evolution with f_{R0}, β_3 to adapt the height of the relative abundance peak and α_4 to adjust the redshift evolution. This is done via minimization of the Gaussian log-likelihood

$$\ln \mathcal{L} = -\frac{1}{2}\left(\mathbf{N}^{\rm theo} - \mathbf{N}^{\rm sim}\right)\mathbf{C}^{-1}\left(\mathbf{N}^{\rm theo} - \mathbf{N}^{\rm sim}\right)^T - \frac{1}{2}\ln\det\mathbf{C}^{-1}, \tag{52}$$

where the covariance matrix consists of a Poissonian contribution and a sample variance term

$$C_{ij}^{-1} = \delta_{ij}N_i^{\rm theo} + b_i b_j N_i^{\rm theo} N_j^{\rm theo}\sigma(V_{\rm box}) \tag{53}$$

with theoretical cluster counts $N_i^{\rm theo}$ per mass bin i and $\sigma(V_{\rm box})$ is the variance of the linear density field computed inside the box. We calculate the mean bias averaged over a bin ΔM_i as

$$\bar{b}_i = \int_{\Delta M_i} {\rm d}M \frac{{\rm d}n}{{\rm d}M} b(M) \Big/ \int_{\Delta M_i} {\rm d}M \frac{{\rm d}n}{{\rm d}M}, \tag{54}$$

using equation (51) for the bias and equation (41) for the mass function. Note that the barrier shape given by $D_{\rm B}$ and β is very important for the proper GR limit, but largely cancels in equation (41). The mass function ratio is therefore almost completely independent from the fiducial barrier values. So while we choose to work within a consistent framework with a mass function that is

Table 3. Best-fitting parameters for the width $D_{\rm B}$ and the drift β of the fiducial GR barrier and the calibrated values for the modified gravity threshold $\delta_{\rm c}(f_{R0}, z)$ in equation (36). The fit was obtained using the dark matter simulations without neutrinos described in Section 3.

GR		$f(R)$			
$D_{\rm B}$	β	α_4	β_3	μ_1	μ_2
0.37(1)	0.11(1)	0.067(1)	$5.6(1)\times10^{-3}$	1.38(1)	21.32(1)

extended to $f(R)$, one could also replace $f_x^{\rm GR}$ in equation (41) with another multiplicity function such as ones by Tinker et al. (2008) or Crocce et al. (2010) as long as it is also calibrated to M_{200m}. We do not perform a comprehensive comparison of mass functions here, but we note that our results for bias and multiplicity agree within ∼5 per cent with those established results in the literature – a value we take as an estimate for current systematic effects on the halo-mass function mainly due to differences in halo definition.

Within our simulations, we find no preference for any redshift evolution in the GR barrier parameters $D_{\rm B}$ and β. We fit them to our ΛCDM simulations first and keep them fixed while calibrating the remaining $f(R)$ parameters α_4, β_3, μ_1, and μ_2 to our fR4, fR5, and fR6 simulations. The resulting best-fitting values with statistical errors are shown in Table 3. For the ΛCDM barrier values we find qualitative agreement with previous similar studies (Maggiore & Riotto 2010b; Kopp et al. 2013; Achitouv et al. 2016), while the position and evolution of the screening mass m_b given by the other parameters deviates substantially from the virial mass function from Kopp et al. (2013). The results are compared to our simulated catalogues in Fig. 7 for a wide range of redshifts and values of $|f_{R0}|$. We find that our model for the halo-mass function can reproduce the simulated data by fitting only four parameters to account for the full non-linear behaviour of the modified gravity model.

The next step is to test the inclusion of neutrinos into our framework via equation (47). We show the combined effect of neutrinos and modified gravity measured from our simulations in Fig. 8 – note that the simulations including neutrinos were not used to fit the mass function parameters. Both cosmologies show an approximate degeneracy leading to an abundance of clusters that is within 10 per cent consistent with ΛCDM expectation at $z = 0$, and the behaviour is well captured by our mass function. This cancellation weakly depends on redshift, so cosmologies with similar mass functions at $z = 0$ will in general differ at earlier times. The precise degeneracy depends on the survey specifications such as redshift range and selection function, and we will return to this problem within the full cosmological parameter space in the next section.

5 FORECASTS

To assess if differences in the cluster abundance are measurable, it is important to consider the changes in the halo-mass function in the context of a survey with a specific selection function.

We now show with two idealized test cases the consequences of our results for the ability of current and future surveys to constrain $|f_{R0}|$. The abundance of clusters is mostly sensitive to $(\Omega_{\rm m}, \sigma_8, \sum m_\nu, \log f_{R0})$; as for the other relevant cosmological parameters, we include priors from different probes. This has to be done with caution, because data sets might show different results when analysed in a $f(R)$ framework. We therefore make use of the fact that the model reproduces a ΛCDM expansion history and limit ourselves to *geometrical* probes.

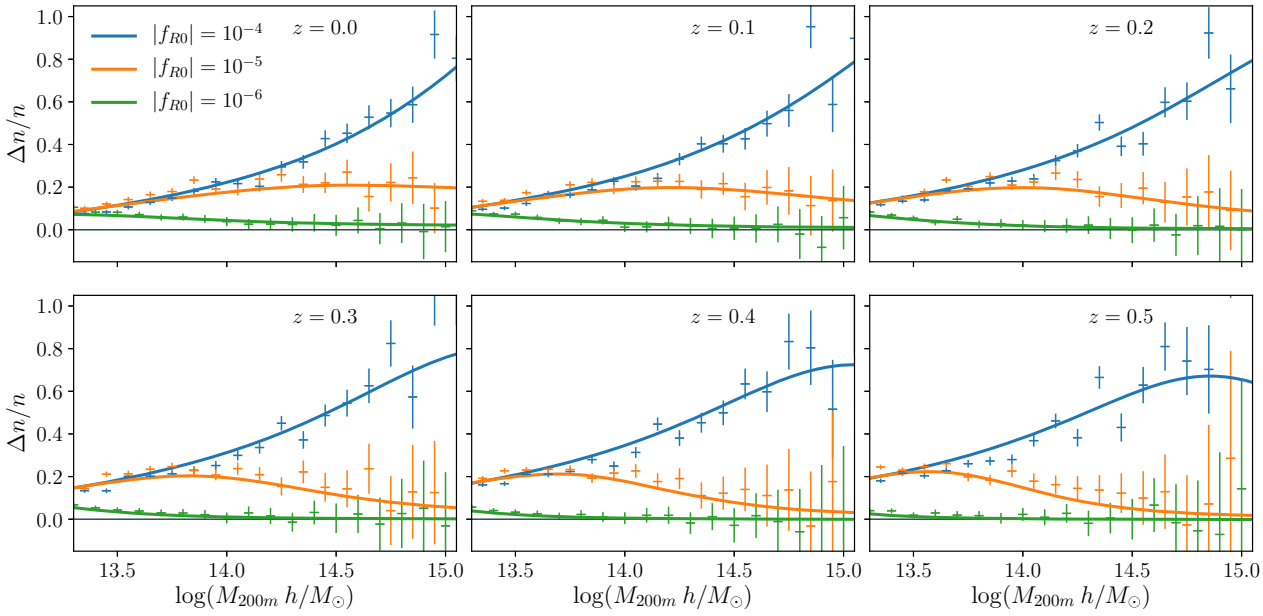

Figure 7. Calibrated halo-mass function ratio for various redshifts and $|f_{R0}| = 10^{-4}$ (blue), 10^{-5} (orange), and 10^{-6} (green) compared to our simulation suite. The $f(R)$ bump in the relative abundance moves towards lower masses with redshift.

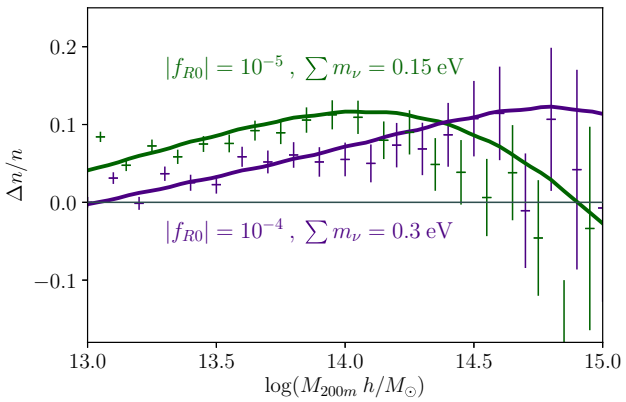

Figure 8. Joint effect of modified gravity and neutrinos on the relative halo abundance at $z = 0$. The theoretical abundance is calculated by combining the calibrated $f(R)$ barrier with the neutrino rescaling (equation 45). Both cluster abundance predictions deviate by less than 10 per cent from the ΛCDM predictions. Data points are from our simulations with Poissonian error bars.

We add baryon acoustic oscillation priors on the distance scale $D_V(z)$ based on BOSS DR12 data (Alam et al. 2017) at redshifts $z = 0.38$, 0.51, and 0.61. We centre them on the same fiducial cosmology used for the simulations described in Section 3 and assume pre-reconstruction errors on the data points, i.e. without assuming a ΛCDM model to linearize the BAO signal, which results in conservative results. We denote this data set with BAO. Complementary, big-bang nucleosynthesis (BBN) measurements constrain the baryon density $\Omega_b h^2$ in the early Universe, where we assume $f(R)$ effects to be negligible – even though this does not have to be the case, and has to be investigated for a given $f(R)$ model carefully (see e.g. Erickcek et al. 2013, 2014). The width of the error bar is based on Cooke et al. (2014). We give a summary of both sets of Gaussian priors in Table 4.

Table 4. A summary of the complementary BAO and BBN mock data sets used in combination with cluster counts if indicated. We assume these result in Gaussian priors on the measured quantity with mean μ and width σ.

Probe	Quantity	μ	σ
BAO	$D_V(z = 0.38)/r_s$	10.05	0.17
	$D_V(z = 0.51)/r_s$	12.84	0.13
	$D_V(z = 0.61)/r_s$	14.77	0.13
BBN	$100 \times \Omega_b h^2$	2.224	0.046

The most powerful complementary data set comes from the CMB. If indicated, we combine the cluster data with priors on the primary CMB parameters derived from the Planck-high-ℓ temperature power spectrum. We use the publicly available chains either for the base model or including varying neutrino masses to derive the covariance matrix and use this multivariate Gaussian prior, again centred on our fiducial cosmology. While changes to the temperature anisotropy power spectrum by $f(R)$ gravity are introduced via the integrated Sachs-Wolfe effect at late times, the impact on multipoles $\ell > 30$ is very small for the relevant parameter space.

5.1 Optical cluster surveys

We now explore these effects in the context of a forecast for an optical cluster survey, where the main observable is the cluster richness λ. We model the expected cluster abundance per bin in redshift Δz_i and richness $\Delta\lambda_j$ as

$$\langle N_{ij}\rangle = \Omega \int_{\Delta z_i} \mathrm{d}z \frac{\mathrm{d}V}{\mathrm{d}z} \int_0^\infty \mathrm{d}M \frac{\mathrm{d}n}{\mathrm{d}M} \int_{\Delta\lambda_j} \mathrm{d}\lambda\; p(\lambda|M)\,, \tag{55}$$

where the survey area Ω is fixed, and introduce the probability $p(\lambda|M)$ for a cluster of mass M to be observed with a richness λ. We assume a lognormal distribution, which allows us to solve the

integration over the observable to arrive at

$$\langle N_{ij}\rangle = \Omega \int_{\Delta z_i} \mathrm{d}z \frac{\mathrm{d}V}{\mathrm{d}z} \int_0^\infty \mathrm{d}M \frac{1}{2}(\mathrm{erfc}(x_{\mathrm{min},j}) - \mathrm{erfc}(x_{\mathrm{max},j})) \frac{\mathrm{d}n}{\mathrm{d}M}\,, \tag{56}$$

with

$$x_{\mathrm{min/max},j} \equiv \frac{\ln\lambda_{\mathrm{min/max},j} - \langle \ln\lambda\rangle(M)}{\sqrt{2\sigma^2_{\ln\lambda}}}\,. \tag{57}$$

We use the weak-lensing calibrated M–λ relation measured by Murata et al. (2018) on SDSS clusters:

$$\langle \ln\lambda\rangle(M) = A + B\ln\left(\frac{M}{M^\star}\right), \tag{58}$$

$$\sigma_{\ln\lambda}(M) = \sigma_0 + q\ln\left(\frac{M}{M^\star}\right), \tag{59}$$

where $M^\star = 3\times10^{14}\,\mathrm{M}_\odot\,h^{-1}$ is the pivot mass of the relation and A, B, σ_0, and q are free parameters varied within priors given by the measurements by Murata et al. (2018). Note that the weak lensing mass estimate of a given cluster is not affected by $f(R)$ because geodesics are unchanged up to a negligible factor $1 + |f_{R0}|$ (Schmidt 2009).

In addition to these observational uncertainties, also the mass function measured in simulations shows systematic scatter. This is mainly caused by ambiguities in the halo definition, so even an identical underlying dark matter field can result in slightly different halo statistics. Typically, different halo finders vary in the resulting amplitude and tilt of the mass function (Knebe et al. 2011), so we assume

$$\frac{\mathrm{d}n}{\mathrm{d}M} \to \frac{\mathrm{d}n}{\mathrm{d}M}\left(\gamma + \eta\log\left(\frac{M}{M^\star}\right)\right) \tag{60}$$

with γ and η free to vary with Gaussian priors with width $\sigma = 0.05$ centred at 1 and 0, respectively. Because these systematic errors are by far larger than statistical uncertainty in our fit of barrier parameters, we keep the latter fixed.

The selection function is crucial for the specific degeneracy between parameters, so we distinguish two cases: either a large, shallow layout or a deeper survey focused on a smaller sky area.

For the shallow case, we assume an area of 10^4 deg^2 with eight richness bins as in Murata et al. (2018) $\lambda \in [20, 25, 30, 35, 40, 47.5, 55, 77.5, 100]$ and one redshift bin $z \in [0.1, 0.3]$. This translates to an approximately flat limiting mass of $M_{\mathrm{min}} \sim 10^{14.4}\,\mathrm{M}_\odot\,h^{-1}$. All bins are well populated with over 100 clusters so we assume a Gaussian likelihood as in equation (52). This mock survey is combined with either CMB or BAO + BBN priors as given in Table 4 and we evaluate the resulting likelihood using the Monte Carlo Markov Chain code `montepython` (Audren et al. 2013; Brinckmann & Lesgourgues 2018).

We show the cluster count distribution in redshift and richness for a shallow survey in Fig. 9. For the given selection function, at low redshifts the effects of neutrinos and modified gravity are almost completely degenerate. Both roughly translate into a shift in the overall amplitude that is also easily mimicked by the amplitude of the M–λ relation. The richness information does help to break this degeneracy slightly because neutrinos tend to cause a strong suppression of very massive clusters while modified gravity leads to a higher abundance of low- and intermediate-mass objects. The resulting limits on $|f_{R0}|$ that can be achieved with such a survey are shown in Table 5. If cluster counts are only combined with BAO information, the limits are rather weak and when adding neutrinos we find no relevant upper bound. Adding the CMB improves the situation by pinning down the other cosmological parameters, but even then adding neutrinos weakens the bounds considerably. Note that there is a small additional effect due to broader CMB constraints on other parameters in a νCDM cosmology, but this mostly extends the contours in the direction of larger allowed Ω_{m} values while $|f_{R0}|$ is anticorrelated with the matter density.

For the deep survey, we take an area of 5000 deg^2 – the total area that will be covered by the Dark Energy Survey[3] – and bins in richness $\lambda \in [20, 30, 45, 60, 200]$ and redshift $z \in [0.2, 0.35, 0.5, 0.65, 0.8]$. The resulting cluster counts for this configuration in redshift and richness are shown in Fig. 10. Information about the abundance at higher redshifts helps to disentangle the competing effects: while neutrinos suppress the population there, the $f(R)$ mass function reverts to GR for $z > 0.5$. Even though modified gravity boosts the abundance of high-mass clusters at low redshifts as shown in Fig. 7, integrated over z the effect on low-richness clusters is dominant as shown in the right-hand panel of Fig. 10. Neutrinos, on the other hand, suppress the high-mass end of the halo-mass function, so that – when combined – the two effects largely break the degeneracy between $f(R)$ and neutrinos. Even without adding CMB information, such a survey can constrain $|f_{R0}|$ down to the effective cluster floor of $\sim10^{-6}$ even when marginalizing over neutrino mass. We show the resulting posterior from both surveys combined with BAO and BBN priors for vanishing neutrino mass in Fig. 11.

5.2 SZ Cluster surveys

The thermal Sunyaev–Zeldovitch (SZ) effect is the heating of CMB photons by scattering with hot electron plasma in clusters of galaxies, leading to a characteristic distortion of the blackbody spectrum (for a review see e.g. Carlstrom, Holder & Reese 2002). The measured amplitude is expressed by the Compton y-parameter and is given by the integrated electron density n_{e} weighted with their temperature T_{e} along the line of sight

$$y \propto \int n_{\mathrm{e}} T_{\mathrm{e}} \mathrm{d}l \propto M\langle T_{\mathrm{e}}\rangle. \tag{61}$$

If we assume a virialized system, $\langle T_{\mathrm{e}}\rangle \propto M^{2/3}$ and the amplitude scales as $y \propto M^{5/3}$. The potential energy of such a cluster is given by

$$\langle E_{\mathrm{pot}}\rangle \propto -\frac{GM^2}{R} \propto -GM^{5/3} \propto -y; \tag{62}$$

therefore, the thermal SZ effect is a probe of the potential energy. In unscreened $f(R)$ gravity, potentials are deeper by a factor of 4/3 and thus a cluster with the same mass will induce a larger SZ signal compared to a standard cosmology.

A SZ-selected cluster sample will hence show a higher abundance in modified gravity both due to the mass function enhancement discussed so far, but also due to modifications of the selection function because lower mass clusters will surpass the detection threshold (Mak et al. 2012).

To model this effect, we consider the relative strength of gravity

$$g(r) \equiv \frac{\mathrm{d}\psi/\mathrm{d}r}{\mathrm{d}\psi_N/\mathrm{d}r} \tag{63}$$

normalized by the Newtonian expectation ψ_{N} that varies between 1 in the screened regime and 4/3 for the unscreened case. From this,

[3] https://www.darkenergysurvey.org

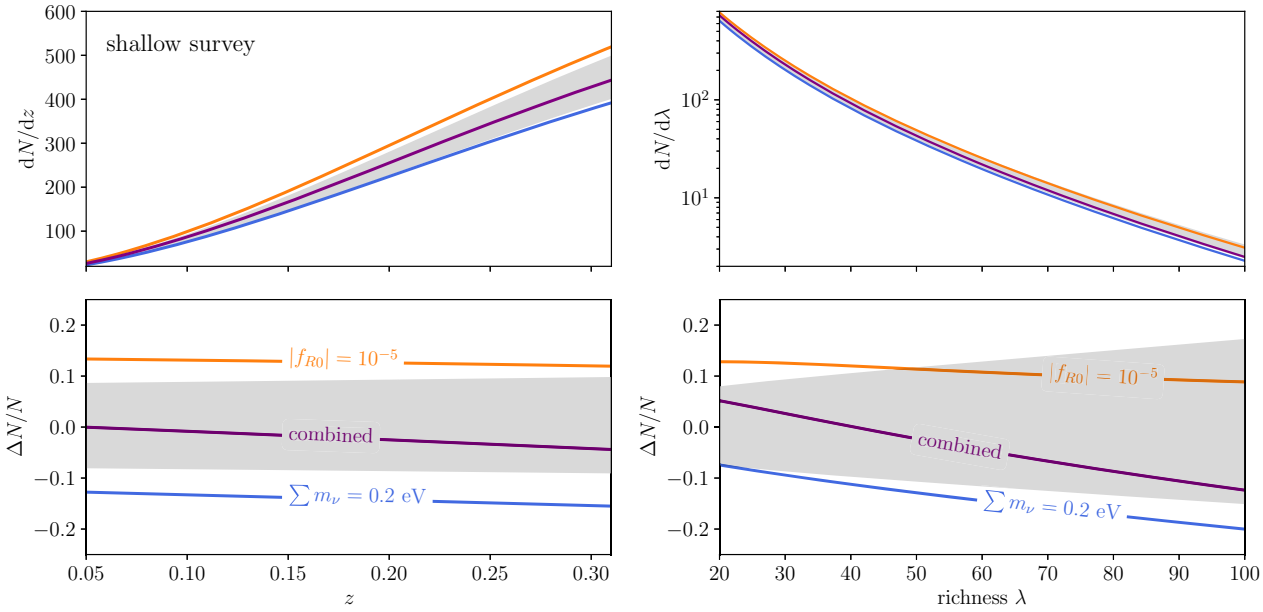

Figure 9. Left: Redshift evolution of the expected cluster abundance for the fiducial cosmology observed by the shallow optical survey described in the text. Grey shaded bands indicate 1σ uncertainty in the mass-richness-relation obtained by drawing samples from the joint distribution $p(A, B, \sigma_0, q)$ while keeping the cosmology fixed. The bottom plot shows relative deviations from ΛCDM caused by modified gravity (orange), massive neutrinos (blue), or both (violet). For low redshifts with the given selection function, both effects are approximately a shift in total amplitude of the counts. Right: Richness distribution of cluster counts. The bottom plot shows relative deviations.

Table 5. Expected constraints on $f(R)$ for either a shallow optical cluster survey spanning $z \in [0.1, 0.3]$ and covering 10^4 deg^2 or a deep survey $z \in [0.2, 0.8]$ with an area of 5000 deg^2. See the main text for a detailed description. The given limit refers to 95 per cent confidence intervals. Note that the external CMB prior does not improve the limit for the deep survey configuration.

Survey	External probes	$\sum m_\nu$	Limit on $\lvert f_{R0}\rvert$
Shallow	BAO+BBN	–	$<8.1 \times 10^{-4}$
	BAO+BBN	Free	–
	BAO+BBN+CMB	–	$<7.6 \times 10^{-5}$
	BAO+BBN+CMB	Free	$<1.5 \times 10^{-4}$
Deep	BAO+BBN	–	$<1.9 \times 10^{-6}$
	BAO+BBN	Free	$<2.0 \times 10^{-6}$

we can derive the weighted average

$$\bar{g} = \frac{\int \mathrm{d}r r^2 w(r) g(r)}{\int \mathrm{d}r r^2 w(r)}, \tag{64}$$

with the weighting function

$$w(r) = \rho(r) r \frac{\mathrm{d}\psi_N}{\mathrm{d}r} \tag{65}$$

which corresponds to the averaged additional potential energy. We follow Schmidt (2010) and make the simplified assumption that the fifth force is only sourced by mass outside of the radius given by equation (12). Therefore, we write

$$g(r) = 1 + \frac{1}{3}\frac{M(<r) - M(<r_{\rm screen})}{M(<r)}, \tag{66}$$

where $r_{\rm screen}$ is the radius where the equality in equation (12) holds. The time evolution of $r_{\rm screen}$ and subsequently $\bar{g}$ is induced by the background evolution of f_R

$$\bar{f}_R(z) = |f_{R0}| \frac{1 + 4\frac{\Omega_\Lambda}{\Omega_{\rm m}}}{(1+z)^3 + 4\frac{\Omega_\Lambda}{\Omega_{\rm m}}}, \tag{67}$$

and the integrals in equation (64) can be solved by assuming NFW profiles so both density and potential are determined. Note that $\bar{g}$ is only very weakly sensitive to the concentration of the profiles, so we fix the relation to the results of Bullock et al. (2001). Even though haloes tend to be more concentrated in $f(R)$ cosmologies (Lombriser et al. 2012b; Shi et al. 2015), this does not change our qualitative argument.

From equation (62), we therefore expect the mass estimate to be biased compared to GR by

$$M_{\rm eff} = \bar{g}^{3/5} M_{\rm true}; \tag{68}$$

that is, the SZ signal coming from an unscreened cluster of fixed mass is higher by a factor of $(4/3)^{3/5} \simeq 1.19$ compared to the GR expectation, while for a screened cluster $\bar{g} = 1$. Similar arguments have been used before to constrain $f(R)$ by comparing lensing masses with X-ray (Wilcox et al. 2015) or dynamical mass estimates (Pizzuti et al. 2017). Here, we want to incorporate the effect into a cluster abundance framework.

To illustrate the method, we consider the consequences for the Planck SZ cluster sample (Planck Collaboration XXIV 2016b). There, the hydrostatic mass bias $(1 - b)$ is introduced to account for the difference between masses inferred from lensing and the corresponding hydrostatic SZ signal. In $f(R)$, we therefore expect $(1 - b)$ to be modified by an additional factor $\bar{g}^{3/5}$. Because the mass definition used in SZ surveys is typically M_{500c}, we calculate NFW potentials to determine $\bar{g}$ using this mass definition and we consider a cluster fully screened if the equality in equation (12) has not been met at R_{500c}.

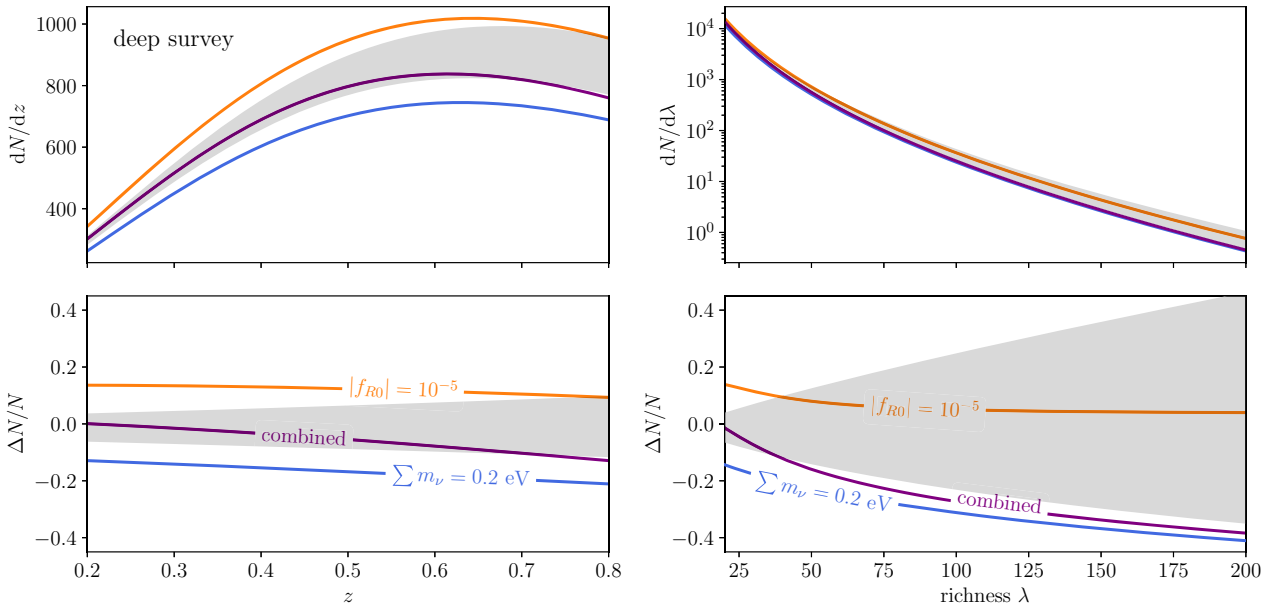

Figure 10. Left: Redshift evolution of the expected cluster abundance for the fiducial cosmology observed by the deep optical survey described in the text. Grey-shaded bands indicate 1σ uncertainty in the mass-richness relation obtained by drawing samples from the joint distribution $p(A, B, \sigma_0, q)$ while keeping the cosmology fixed. The bottom plot shows relative deviations from ΛCDM caused by modified gravity (orange), massive neutrinos (blue), or both (violet). While degenerate at low redshifts, neutrino effects are more pronounced at high z [where the $f(R)$ mass function reverts to GR]. Right: Richness distribution of cluster counts. The bottom plot shows relative deviations. The degeneracy here crucially depends on the position of the $f(R)$ peak in the relative abundance.

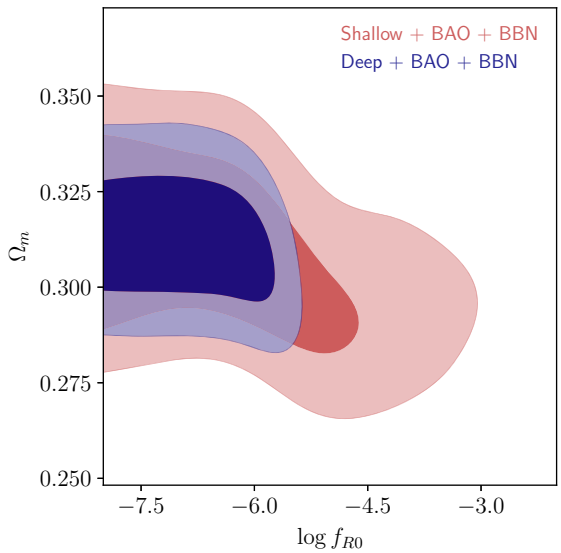

Figure 11. Expected constraints on $|f_{R0}|$ from a shallow or deep optical cluster survey as described in the text. The contours shown here assume vanishing neutrino mass.

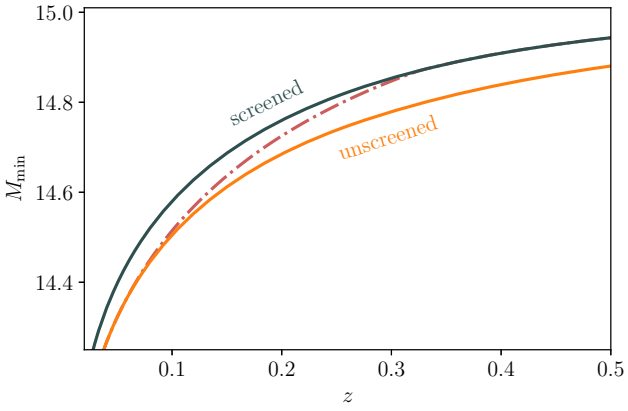

Figure 12. Limiting mass using the Planck SZ cluster selection function for the fiducial case (grey), assuming all clusters are unscreened for a high value of $|f_{R0}| = 10^{-4}$ (orange) and an intermediate case where parts of the sample are screened with $|f_{R0}| = 5 \times 10^{-5}$ (red, dot–dashed).

The limiting mass is determined according to the procedure described in Planck Collaboration XXIV (2016b) as the mass of an object with detection probability 1/2 by using the measured noise maps, the SZ–scaling relations given there and by applying a signal-to-noise detection threshold of $q = 6$.

In Fig. 12, we show the resulting limiting mass for the Planck SZ selection function. Because the clusters in the sample are very massive, they are screened unless $|f_{R0}|$ reaches quite high values $\sim 10^{-4}$. However, if all clusters in the Planck sample are unscreened, this would be completely absorbed by the fiducial measurement of the bias factor – but because the lensing calibration is performed on very massive objects, smaller objects can still exhibit deviations. This is illustrated with the dot–dashed line for $|f_{R0}| = 5 \times 10^{-5}$.

The resulting Planck SZ cluster counts are shown in Fig. 13. Here, we recalibrate our mass function to M_{500c} using the rescaling outlined in Hu & Kravtsov (2003). While this simplified procedure will not predict the position of the screening mass and the subsequent position of the $f(R)$ peak in the mass function correctly, we just want to point out that the effect of the adjusted selection function can be quite large – in this case, the additional observed cluster abundance caused by the higher SZ signal from low-mass clusters (dashed lines in Fig. 13) contributes almost in equal parts to the higher total observed cluster counts caused by the higher intrinsic abundance in the mass function itself (solid lines).

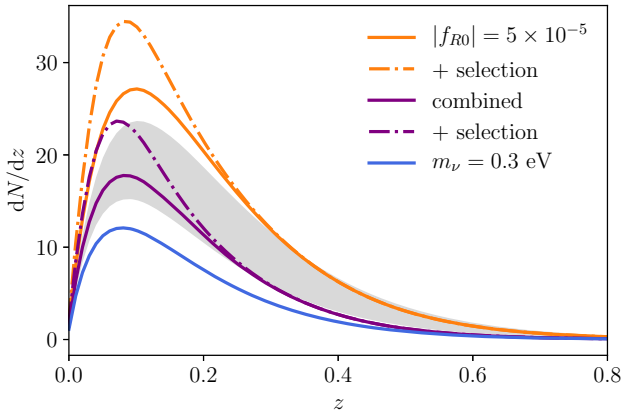

Figure 13. Redshift distribution for the Planck cluster counts using the modified halo-mass function (solid) and also taking selection function effects into account via equation (68) (dot–dashed). Grey bands indicate a 10 per cent uncertainty in the cluster mass scale $(1 - b)$. The enhancement of the observed cluster abundance in $f(R)$ due to the boosted abundance of massive clusters in the mass function (orange solid) is comparable to the number of low-mass objects that surpass the detection threshold due to the higher SZ signal caused by the enhancement of gravity (orange dashed).

The high-mass scale for the Planck clusters limits the usefulness of this method here, but upcoming X-ray surveys such as *eRosita*[4] are expected to detect clusters and groups down to $M \sim 10^{13}\,\mathrm{M}_\odot\,h^{-1}$, where a similar analysis can prove to be very powerful.

5.3 Searching for modified gravity with other parametrizations

The problem in searching for modifications of gravity is that theory space is enormous, and there are potentially many models to test. Current and future cosmological surveys are mostly designed to search for deviations in the dark energy equation of state w from -1, so we might wonder if these standard searches are sufficient to detect deviations from ΛCDM without assuming a specific model. The hope is then that once an anomaly is detected (for example, an equation of state $w \neq -1$), one can resolve the tension in an extended model involving new physics.

As a test case, we set $\sum m_\nu = 0$ and generate a fiducial cluster catalogue with $|f_{R0}| = 10^{-4}$ for the shallow optical cluster survey described above combined with CMB and BAO+BBN information. This value of $|f_{R0}|$ is larger than the 95 per cent upper limit $|f_{R0}| < 7.2 \times 10^{-5}$ from the same combination of data sets given in Table 5 and could be detected by a dedicated search using the correct analysis model. We then explore the posterior assuming a wCDM model and use the corresponding CMB covariance matrix to obtain our prior. For this analysis, we assume that the effect of w on the mass function is captured by the different evolution of the density field alone and therefore use the ΛCDM barrier parameters.

We find that the best-fitting wCDM model does not show any significant deviations from the vanilla case. The full posterior distribution of the major cosmological parameters is shown in Fig. 14, and while there are small deviations in the nuisance parameters, all of them are within 1σ compatible with their standard values without any peculiar features.

[4] http://www.mpe.mpg.de/eROSITA

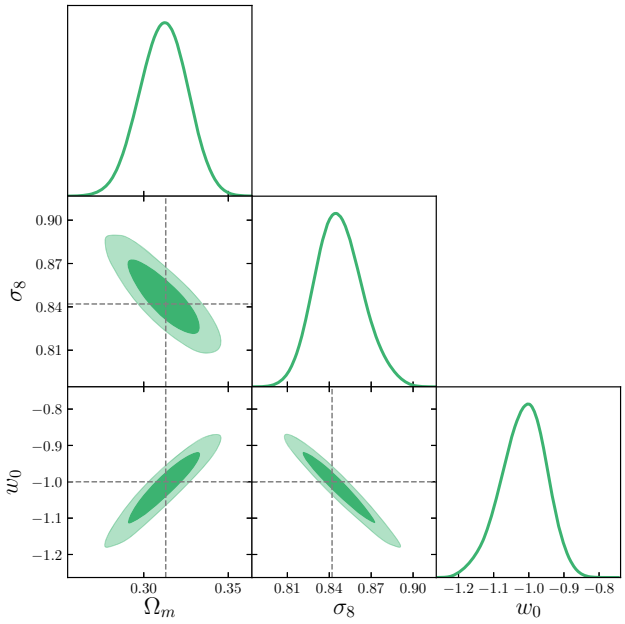

Figure 14. Posterior distribution of the main cosmological parameters for the shallow survey +BBN+BAO+CMB with a fiducial model generated using $|f_{R0}| = 10^{-4}$. All parameters are fully consistent with a vanilla ΛCDM model and none of these (including nuisance parameters not plotted here) show significant deviations $>1\sigma$ from their fiducial values indicated by dashed lines.

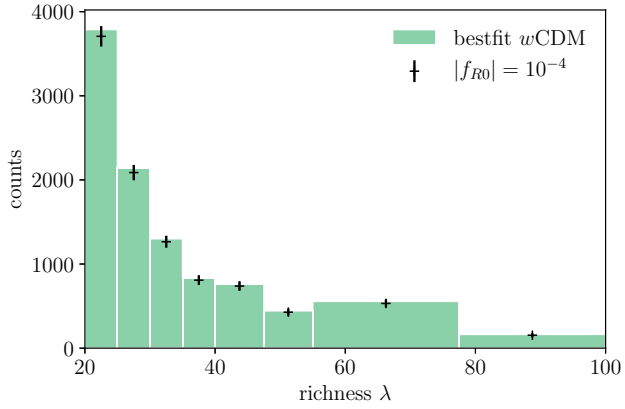

Figure 15. Bars show the binned richness distribution of clusters for the best-fitting wCDM model compared to the fiducial data points generated with $|f_{R0}| = 10^{-4}$. All cosmological parameters for the best-fitting model are very close to ΛCDM (see also Fig. 14) and all nuisance parameters agree within 1σ with their fiducial values.

We also compare the richness distribution of cluster counts for the best-fitting model with the $f(R)$ mock data in Fig. 15 and find no significant deviations. The full parameter space proves to be flexible enough to account even for a large value of $|f_{R0}|$ that could be detected if the correct model is assumed in the analysis, where the nuisance parameters make up for most of the difference between the models since a varying equation of state alone does not mimic the $f(R)$ signal – even though all of them remain within 1σ range of their fiducial values. This indicates that wCDM might not be a good approach to search for generic deviations from ΛCDM for models that are not captured by this particular paramtrization.

Therefore, we cannot necessarily exclude modified gravity (or other) models just from the lack of tensions in the ΛCDM or wCDM analysis of cosmological surveys. Instead, it is necessary to consider the phenomenology of models individually in order to exclude them.

6 CONCLUSIONS

In this paper, we presented an accurate halo-mass function based on a spherical collapse framework valid for modified gravity and neutrino cosmologies, and calibrated it to a suite of specifically designed cosmological simulations, the DUSTGRAIN-*pathfinder* runs. This allows joint constraints from cluster abundance studies. We keep the additional relative change and the fiducial GR mass function separate, so our results can be used with any other mass function calibrated to our mass definition of M_{200m}.

The cluster mass definition is crucial to accurately predict the characteristic $f(R)$ peak in the relative abundance because it governs the onset of screening effects. Mass functions for other commonly used mass definitions such as M_{500c} therefore require recalibration of the screening mass, which we refer to future work.

We also demonstrate that the inclusion of neutrinos via a rescaling of the density field equation (43) still holds in extended models, and we find a degeneracy between effects of $f(R)$ and massive neutrinos in the abundance of clusters that limits the ability of surveys with small redshift reach to disentangle them. This is likely to weaken existing limits on $|f_{R0}|$ from cluster abundance, and we will use the mass function for joint constraints using cluster data in a follow-up paper.

Deeper cluster surveys however can tell neutrinos and modified gravity reliably apart by their different redshift evolution, and future optical cluster samples will be able to probe the entire phenomenologically relevant parameter range of the model even when accounting for systematic uncertainties. This could be realized by the complete Dark Energy Survey, *eRosita*, or *Euclid*[5] cluster samples.

We also explore the possibility to include $f(R)$ effects in the selection function of SZ or X-ray surveys directly as proposed by Schmidt (2010) and we find potentially large effects if the sample can be extended to include nearby, intermediate, and low-mass objects with $M \lesssim 10^{14}\,\mathrm{M}_\odot\,h^{-1}$. Even though neutrinos can mask the additional abundance in the mass function at low redshifts, it is still possible to detect fifth forces through these selection effects. This allows to incorporate the limits on $|f_{R0}|$ from comparing lensing mass estimates and X-ray, SZ, or dynamical mass estimates consistently into cluster abundance studies in a fully consistent framework.

Finally, we find that generic searches for wCDM do not necessarily lead to significant tensions or conspicuous features when used to analyse mock $f(R)$ data – even if the value of $|f_{R0}|$ could be detected with the same data set in a dedicated analysis. This emphasizes the need to model phenomenology of ΛCDM extensions carefully. A lack of tensions within a parametrization does not imply the absence of new physics.

ACKNOWLEDGEMENTS

Most cosmological quantities in this paper were calculated using the Einstein–Boltzmann code `class` (Blas, Lesgourgues & Tram 2011).

SH wants to thank Vanessa Böhm and Korbinian Huber for many helpful discussions. We appreciate the help of Ben Moster with cross-checks for our simulation suite. JW and SH acknowledge the support of the DFG Cluster of Excellence 'Origin and Structure of the Universe' and the Transregio programme TR33 'The Dark Universe'. MB acknowledges support from the Italian Ministry for Education, University and Research (MIUR) through the SIR individual grant SIMCODE (project number RBSI14P4IH), from the grant MIUR PRIN 2015 'Cosmology and Fundamental Physics: illuminating the Dark Universe with Euclid', and from the agreement ASI n.I/023/12/0 'Attività relative alla fase B2/C per la missione Euclid'. The DUSTGRAIN-*pathfinder* simulations discussed in this work have been performed and analysed on the Marconi supercomputing machine at Cineca thanks to the PRACE project SIMCODE1 (grant no. 2016153604) and on the computing facilities of the Computational Centre for Particle and Astrophysics (C2PAP) and the Leibniz Supercomputing Centre (LRZ) under the project ID pr94ji.

[5] https://www.euclid-ec.org/

REFERENCES

Achitouv I., Baldi M., Puchwein E., Weller J., 2016, Phys. Rev. D, 93, 103522
Alam S. et al., 2017, MNRAS, 470, 2617
Allen S. W., Evrard A. E., Mantz A. B., 2011, ARA&A, 49, 409
Araki T. et al., 2005, Phys. Rev. Lett., 94, 081801
Arnold C., Puchwein E., Springel V., 2015, MNRAS, 448, 2275
Arnold C., Springel V., Puchwein E., 2016, MNRAS, 462, 1530
Arnold C., Fosalba P., Springel V., Puchwein E., Blot L., 2019, MNRAS, 483, 790
Audren B., Lesgourgues J., Benabed K., Prunet S., 2013, JCAP, 1302, 001
Baldi M., Villaescusa-Navarro F., 2018, MNRAS, 473, 3226
Baldi M., Villaescusa-Navarro F., Viel M., Puchwein E., Springel V., Moscardini L., 2014, MNRAS, 440, 75
Bardeen J. M., Bond J. R., Kaiser N., Szalay A. S., 1986, ApJ, 304, 15
Battye R. A., Weller J., 2003, Phys. Rev. D, 68, 083506
Baumann D., Beutler F., Flauger R., Green D., Vargas-Maga na M., Slosar A., Wallisch B., Yèche C., 2018, preprint (arXiv:1803.10741)
Baxter E. J., Rozo E., Jain B., Rykoff E., Wechsler R. H., 2016, MNRAS, 463, 205
Blas D., Lesgourgues J., Tram T., 2011, J. Cosmology Astropart. Phys., 7, 034
Bond J. R., Cole S., Efstathiou G., Kaiser N., 1991, ApJ, 379, 440
Brinckmann T., Lesgourgues J., 2018, preprint (arXiv:1804.07261)
Bullock J. S., Kolatt T. S., Sigad Y., Somerville R. S., Kravtsov A. V., Klypin A. A., Primack J. R., Dekel A., 2001, MNRAS, 321, 559
Carlstrom J. E., Holder G. P., Reese E. D., 2002, ARA&A, 40, 643
Castorina E., Sefusatti E., Sheth R. K., Villaescusa-Navarro F., Viel M., 2014, J. Cosmology Astropart. Phys., 2, 049
Cataneo M. et al., 2015, Phys. Rev. D, 92, 044009
Cataneo M., Rapetti D., Lombriser L., Li B., 2016, J. Cosmology Astropart. Phys., 12, 024
Cooke R. J., Pettini M., Jorgenson R. A., Murphy M. T., Steidel C. C., 2014, ApJ, 781, 31
Corasaniti P. S., Achitouv I., 2011, Phys. Rev. Lett., 106, 241302
Costanzi M., Villaescusa-Navarro F., Viel M., Xia J.-Q., Borgani S., Castorina E., Sefusatti E., 2013, J. Cosmology Astropart. Phys., 12, 012
Crocce M., Fosalba P., Castander F. J., Gazta naga E., 2010, MNRAS, 403, 1353
Davis M., Efstathiou G., Frenk C. S., White S. D., 1985, ApJ, 292, 371
Doroshkevich A. G., 1970, Astrophysics, 6, 320
Erickcek A. L., Barnaby N., Burrage C., Huang Z., 2013, Phys. Rev. Lett., 110, 171101
Erickcek A. L., Barnaby N., Burrage C., Huang Z., 2014, Phys. Rev. D, 89, 084074

Giocoli C., Baldi M., Moscardini L., 2018, MNRAS, 481, 2813
Hu W., Kravtsov A. V., 2003, ApJ, 584, 702
Hu W., Sawicki I., 2007, Phys. Rev. D, 76, 064004
Ichiki K., Takada M., 2012, Phys. Rev. D, 85, 063521
Knebe A. et al., 2011, MNRAS, 415, 2293
Kopp M., Appleby S. A., Achitouv I., Weller J., 2013, Phys. Rev. D, 88, 084015
Kravtsov A. V., Borgani S., 2012, ARA&A, 50, 353
Lesgourgues J., Pastor S., 2006, Phys. Rep., 429, 307
Lewis A., Challinor A., Lasenby A., 2000, ApJ, 538, 473
Lombriser L., Slosar A., Seljak U., Hu W., 2012a, Phys. Rev. D, 85, 124038
Lombriser L., Koyama K., Zhao G.-B., Li B., 2012b, Phys. Rev. D, 85, 124054
Lombriser L., Li B., Koyama K., Zhao G.-B., 2013, Phys. Rev. D, 87, 123511
Lombriser L., Koyama K., Li B., 2014, J. Cosmology Astropart. Phys., 3, 021
Lovelock D., 1972, J. Math. Phys., 13, 874
Maggiore M., Riotto A., 2010a, ApJ, 711, 907
Maggiore M., Riotto A., 2010b, ApJ, 717, 515
Mak D. S. Y., Pierpaoli E., Schmidt F., Macellari N., 2012, Phys. Rev. D, 85, 123513
Merten J., Giocoli C., Baldi M., Meneghetti M., Peel A., Lalande F., Starck J.-L., Pettorino V., 2018, MNRAS, preprint (arxiv:1810.11027)
Mohr J. J., O'Shea B., Evrard A. E., Bialek J., Haiman Z., 2003, Nucl. Phys. B Proc. Suppl., 124, 63
Murata R., Nishimichi T., Takada M., Miyatake H., Shirasaki M., More S., Takahashi R., Osato K., 2018, ApJ, 854, 120
Naik A. P., Puchwein E., Davis A.-C., Arnold C., 2018, MNRAS, 480, 5211
Nakamura T. T., Suto Y., 1997, Prog. Theor. Phys., 97, 47,
Paech K., Hamaus N., Hoyle B., Costanzi M., Giannantonio T., Hagstotz S., Sauerwein G., Weller J., 2017, MNRAS, 470, 2566
Peel A., Pettorino V., Giocoli C., Starck J.-L., Baldi M., 2018a, A&A, 619, A38
Peel A., Lalande F., Starck J.-L., Pettorino V., Merten J., Giocoli C., Meneghetti M., Baldi M., 2018b, preprint (arxiv:1810.11030)
Pizzuti L. et al., 2017, J. Cosmology Astropart. Phys., 7, 023
Planck Collaboration et al., 2016a, A&A, 594, A13
Planck CollaborationXXIV, 2016b, A&A, 594, A24
Press W. H., Schechter P., 1974, ApJ, 187, 425
Puchwein E., Baldi M., Springel V., 2013, MNRAS, 436, 348
Roncarelli M., Villaescusa-Navarro F., Baldi M., 2017, MNRAS, 467, 985
Roncarelli M., , Baldi M., Villaescusa-Navarro F., 2018, MNRAS, 481, 2497
Schmidt F., 2009, Phys. Rev. D, 80, 043001
Schmidt F., 2010, Phys. Rev. D, 81, 103002
Schmidt F., Vikhlinin A., Hu W., 2009, Phys. Rev. D, 80, 083505
Sellentin E., Durrer R., 2015, Phys. Rev. D, 92, 063012
Sheth R. K., Tormen G., 1999, MNRAS, 308, 119
Sheth R. K., Tormen G., 2002, MNRAS, 329, 61
Shi D., Li B., Han J., Gao L., Hellwing W. A., 2015, MNRAS, 452, 3179
Springel V., 2005, MNRAS, 364, 1105
Springel V., White S. D. M., Tormen G., Kauffmann G., 2001, MNRAS, 328, 726
Tinker J., Kravtsov A. V., Klypin A., Abazajian K., Warren M., Yepes G., Gottlöber S., Holz D. E., 2008, ApJ, 688, 709
Viel M., Haehnelt M. G., Springel V., 2010, JCAP, 1006, 015
Villaescusa-Navarro F., Banerjee A., Dalal N., Castorina E., Scoccimarro R., Angulo R., Spergel D. N., 2018, ApJ, 861, 53
von Braun-Bates F., Winther H. A., Alonso D., Devriendt J., 2017, J. Cosmology Astropart. Phys., 3, 012
Wilcox H. et al., 2015, MNRAS, 452, 1171
Winther H. A. et al., 2015, MNRAS, 454, 4208
Zennaro M., Bel J., Villaescusa-Navarro F., Carbone C., Sefusatti E., Guzzo L., 2017, MNRAS, 466, 3244

This paper has been typeset from a TEX/LATEX file prepared by the author.